Numerical Studies of Cell Stack for Zinc-Nickel Single Flow Battery

Shouguang Yao[1,], Yunhui Zhao[1], Xiaofei Sun[1], Dapei Ding[1], Jie Cheng[2]*

[1] Jiangsu University of Science and Technology, Zhenjiang 212003, China
[2] Zhangjiagang Smartgrid Fanghua Electrical Energy Storage Research Institute, Zhangjiagang 215600, China
*E-mail: zjyaosg@126.com

A three-dimensional stationary model is established, based on the universal conservation laws and a kinetic model for reaction involving hydroxide and zinc ions, is applied to describe a zinc-nickel single flow battery cells stack. The model is validated against the experimental data and is used to describe the spatial distribution of flow, concentration, current density and potential. The effects of variations in electrolyte flow rate and concentration are further studied. The model results indicate that the current density and potential distribution of each battery cell have good consistency and the influence of the spatial arrangement of battery cells is more clearly reflected in the distribution of flow and concentration. An increase in flow rate or ions concentration leads to a slighter concentration polarization, a better consistency and a higher cell stack voltage.

1. INTRODUCTION

There is an urgent need to develop large-scale energy storage with the vigorous development of renewable energy such as solar and wind energies [1]. Liquid-flow batteries have been regarded as the most suitable technology for large-scale chemical energy storage because of their high reliability, independent output power and capacity, low total-life cost, and zero emission [2].

In the early days, dual-flow batteries accounted for the majority of flow batteries, of which all-vanadium flow batteries(VRBs) were the most representative. Thus, research on flow batteries mainly focused on VRBs [3-4]. Yin [5] proposed a 3D model for VRBs with cross-flow channel design, and two different electrical stack inlet structures were used to determine fluid pressure, potential, current density, and over-potential distribution during battery workup. Zheng [6] constructed a 3D quasi-static

thermal analytical model for VRBs to characterize the spatial distribution of temperature and its quasi-static behavior, and also studied the influence of applied current density, porosity, and liquid flow rate on heat production. Kim and Park [7] recently designed a test system with four VRB units to effectively control temperature and flow of the system, and the electrochemical performance of the battery discharge process was established. With the development of liquid flow battery technology, a new type of single flow battery system developed on traditional lead-acid batteries has attracted much attention, especially zinc-nickel single flow battery [8], which shows a good application prospect due to its good stability and high energy efficiency. The research at present on zinc-nickel single flow battery is mainly based on experimental [9-14]. In the numerical study, Song [15] established a three-dimensional stationary model for zinc-nickel single flow battery cell stack, and analyzed the non-uniformity of the designed flow structure based on the introduced non-uniformity index γ. Liu [16] considered the diffusion and migration of liquid electrolyte and the proton diffusion and ohmic voltage drop inside the solid phase active material, and established a mathematical model for the nickel electrode of zinc-nickel single-liquid battery. Yao [17] established a mathematical model for zinc-nickel single-flow battery cell stack by coupling reaction rate equation and equilibrium potential equation to study the voltage and electrode over-potential during charging, and verify the reliability of the mathematical model by comparing with experimental data. Xiao [18] preliminarily established a three-dimensional stationary model of zinc-nickel single-flow battery to analyze the concentration and current density distributions inside the battery, and investigated the influence of channel width and flow rate.

Based on the work of Xiao [18], a stack model consisting of 23 battery cells is applied to investigate the spatial distributions of flow rate, concentration current density and potential inside the stack, and to study the effects of inlet flow velocity and ion inlet concentration. It will provide a basis for further optimizing the internal structure and operating parameters of zinc-nickel single flow battery.

2. EXPERIMENTAL DETAILS

The experimental object is the second generation zinc-nickel single-flow battery. The positive electrode is a sintered nickel oxide electrode with a size of 240mm×150mm×0.32mm and the negative electrode is an inert current collector with a size of 240mm×150mm×0.08mm. The initial electrolyte was 7000mol/m^3 KOH $+400 \text{mol/m}^3$ $K_2Zn(OH)_4$. The width of channel between the positive and negative electrodes was 3.8 mm. The volume of the electrolyte tank was 5.76L. The equipment used in the experiment mainly includes BTS7.5.X battery test system, data acquisition auxiliary test system, 5V200A-NTFA detector and clip-on ammeter for battery test.

A load cycle of 1h charge, 60s rest, 1h discharge was applied to the battery. During charge or discharge a constant current density corresponding to the average current density in the battery 100A/m2 was applied. The charge cut-off voltage is 2.1V and the discharge cut-off voltage is 1.2V. Under the environment of room temperature 25 ℃, the terminal voltage data of the cell stack during discharge is collected through an auxiliary test system.

3. MODEL DEVELOPMENT

3.1. Model Geometry and Assumptions

The simulation adopts a stack structure as shown in fig.1. The stack consists of 23 two-channel battery cells, which are closely attached to each other and are sequentially from cell 1 to cell 23 in the x direction. In each battery cell, two positive electrodes share a negative electrode, and electrolyte flow channels are arranged between the positive and negative plates. The electrolyte flows in from the bottom trapezoidal flow channel, then flows through the 23 cell flow channels, and finally flows out from the outlet of the upper flow channel. The electrochemical reaction occurs on the solid-phase surface of porous electrode and negative surface. The reaction equations are as follows

Positive： $\qquad$ $2NiOOH + 2H_2O + 2e^- \rightleftarrows 2Ni(OH)_2 + 2OH^-$ $\qquad$ (1)

Negative： $\qquad$ $Zn + 4OH^- \leftrightarrows Zn(OH)_4^{2-} + 2e^-$ $\qquad$ (2)
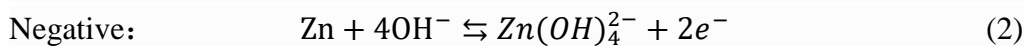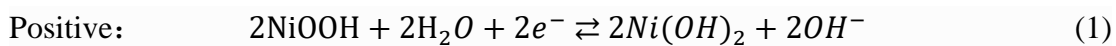
In order to simplify the problem, we made some assumptions:

(1)   The active nickel concentration varying with time determines soc (state of charge). Thus, at a specific active nickel concentration, the dynamic model could be simplified as a stationary one to faster solve without losing much accuracy especially for large geometry;

(2)   Physical properties of electrode and electrolyte are isotropic and homogeneous;

(3)   The electrolyte in the porous electrode is still and its mass transfer does not consider convection term;

(4)   The side reaction of oxygen evolutions is neglected;

(5)   Isothermal and weightless conditions are assumed for all domains.
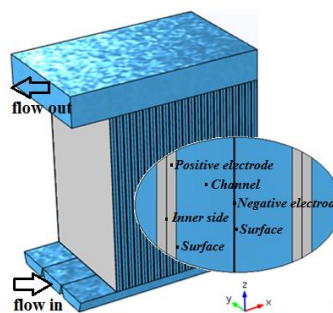
Figure 1. Stack structure schematic.

3.2. Governing Equations

The governing equations based on the approaches developed by Liu [16] and Xiao [18] and some of them are corrected:

Continuity:

$\nabla v = 0$ $\qquad$ (3)

Momentum conservation:

$$\nabla[\mu(\nabla v + (\nabla v)^T)] - \nabla p = \rho(v \cdot \nabla)v \qquad (4)$$

Species conservation:

$$-D_i \nabla c_i - z_i u_{m,i} F c_i \nabla \emptyset_l + v \cdot c_i = S_i \qquad (5)$$

Charge conservation:

$$\nabla i_s = -\nabla i_l = -\sigma_s \nabla^2 \emptyset_s = -\sigma_l \nabla^2 \emptyset_l = S_\emptyset \qquad (6)$$

ρ, denotes the electrolyte density; v, denotes the electrolyte density; D_i, denotes the diffusion coefficient of i; z_i, denotes the charge quantity of i; $u_{m,i}$, denotes the migration rate of i; c_i, denotes the bulk concentration, $i \in \{OH^-, Zn(OH)_4^{2-}\}$; S_i is the source term of species i; $\emptyset_s$ is the potential of solid liquid phase and $\emptyset_l$ is the potential of liquid phase; $S_\emptyset$ is the source term for charge conservation.

The liquid phase diffusion coefficient and solid phase conductivity are corrected according to Bruggemann:

$$\sigma_i^{\text{eff}} = \varepsilon^{1.5} D_i \, , \quad \sigma_s^{\text{eff}} = (1 - \varepsilon)^{1.5} \sigma_s \qquad (7)$$

Where ε is the porosity.

Table 1. Source terms for species in the positive and negative electrodes.

Source terms		Positive electrode	Negative electrode
S_i	OH^-	$-a_e j_1/F$	$2 \times j_2/F$
	$Zn(OH)_4^{2-}$	0	$0.5 \times j_2/F$
S_H	$Ni(OH)_2$	$-a_e j_1/F$	0
$S_\emptyset$	$\emptyset_s$	$a_e j_1$	j_2
	$\emptyset_l$	$-a_e j_1$	$-j_2$

The Butler-Volmer law describes the electrochemical reactions taking place on the surfaces the electrode:

$$j_1 = i_1^0 \left[\frac{c_I}{c_I^{\text{ref}}} \frac{c_{III}}{c_{III}^{\text{ref}}} \exp\left(\frac{\alpha_{1,a}F}{RT}\eta_1\right) - \frac{c_{III}^{\text{max}} - c_{III}}{c_{III}^{\text{max}} - c_{III}^{\text{ref}}} \exp\left(-\frac{\alpha_{1,c}F}{RT}\eta_1\right) \right] \qquad (8)$$

$$j_2 = i_2^0 \left[\left(\frac{c_I}{c_I^{\text{ref}}}\right)^4 \exp\left(\frac{2\alpha_{2,a}F}{RT}\eta_2\right) - \frac{c_{II}}{c_{II}^{\text{ref}}} \exp\left(-\frac{2\alpha_{2,c}F}{RT}\eta_2\right) \right] \qquad (9)$$

j_1 denotes the transfer current densities for the positive electrodes and j_2 denotes the transfer current densities for negative electrodes. i_1^0 and i_2^0 are the exchange current densities. The symbols 'I','II' and 'III', represent the species 'OH^-', '$Zn(OH)_4^{2-}$' and '$Ni(OH)_2$' respectively.

The over-potentials for the positive and negative electrode reactions are defined as:

$$\eta_1 = (\phi_s - \phi_l) - U_1 \qquad (10)$$

$$\eta_2 = (\phi_s - \phi_l) - U_2 \qquad (11)$$

where U_1 and U_2 can be estimated from the relevant Nernst equations:

$$U_1 = U_1^0 + \frac{RT}{F} \ln \frac{c_{III}^{\text{max}} - c_{III}}{c_{III}^{\text{max}}} - \frac{RT}{F} \ln\left(\frac{c_{III}}{c_{III}^{\text{max}}} \cdot \frac{c_I}{c_I^{\text{ref}}}\right) \qquad (12)$$

$$U_2 = U_2^0 + \frac{RT}{2F} \log\left(\frac{c_{II}}{c_{II}^{\text{ref}}}\right) - \frac{2RT}{F} \log\left(\frac{c_I}{c_I^{\text{ref}}}\right) \qquad (13)$$

Where standard potential U_1^0 and U_2^0 (versus Hg/HgO) [11] are listed in Table 4.

Table 2. Electrode Properties

Parameter name	Symbols	Value	Unit
Porosity	ε	0.44	m s^{-1}
Electronic conductivity (Nickel oxide)	σ_s	2.5×10^3	S m^{-1}
Electronic conductivity (Aluminum)	σ_s	1.83×10^7	S m^{-1}
Active specific surface area	a_e	3.864×10^5	m^{-1}
Length	L	240	mm
Thickness (positive)	d_a	0.32	mm
Thickness (negative)	d_c	0.08	mm

Table 3. Electrolyte Properties

Parameter name	Symbols	Value	Unit
Viscosity	μ	0.03139	Pa s
Electrolyte conductivity	σ_l	65	S m^{-1}
Diffusion coefficient	D_1	3.26×10^{-9}	m^2 s^{-1}
Diffusion coefficient	D_2	2×10^{-10}	m^2 s^{-1}
channel width	d_l	3.8	mm

Table 4. Kinetic parameters in the model

Parameter name	Symbols	Value	Unit
Anodic transfer coefficient: positive	$\alpha_{1,a}$	0.5	--
Cathodic transfer coefficient: positive	$\alpha_{2,a}$	0.5	--
Anodic transfer coefficient: negative	$\alpha_{1,c}$	0.5	--
Cathodic transfer coefficient: negative	$\alpha_{2,c}$	0.5	--
Exchange Current Density: Positive	i_1^0	1.04	A m^{-2}
Exchange Current Density: negative	i_2^0	300	A m^{-2}
Equilibrium potential (positive)	U_1^0	0.49	V
Equilibrium potential (negative)	U_2^0	-1.26	V

3.3. Boundary Condition

Boundary conditions are required at all boundaries of the computational domains, as well as at internal interfaces.

3.3.1. Boundary Conditions for Momentum Balance

For the momentum equations, velocity boundary conditions are used at the inlets, pressure boundary conditions are used at the outlets and on all walls the no-slip boundary condition is applied. The detailed expressions are as follows

$$\begin{cases} v = v_{in} \text{(at the inlet)} \\ p = p_{out} \text{(at the outlet)} \\ \nabla P \cdot \vec{n} = 0 \text{(on the wall)} \end{cases} \quad (14)$$

where p_{out} is set to zero and the inlet velocity can be calculated by the following equation

$$v_{in} = \frac{Q}{A} \quad (15)$$

Where A is the area of the stack inlet and Q is the volumetric flow rate.

3.3.2. Boundary Conditions for Species Conservation

In this stationary model, the concentration of all species at inlets are constant

$$\begin{cases} c_I^{in} = c_I^0 \\ c_{II}^{in} = c_{II}^0 \end{cases} \quad (16)$$

Introducing a parameter named soc, which represents the state of charge of the cells stack, the concentration expressions of the active substance at inlets at any given soc will be

$$c_{III} = c_{III}^{max}(1 - soc) \quad (17)$$

Where c_I^0 and c_{II}^0 are the initial hydroxide ion concentration and zinc ion concentration of the stack respectively. c_{III}^{max} denotes the maximum concentration of active substance $Ni(OH)_2$. At the outlets of the stack, the diffusive fluxes of all species are set to zero:

$$-D_i \nabla c_i \cdot \boldsymbol{n} = 0 \quad (18)$$

3.3.3. Boundary Conditions for Charge Conservation

The battery is operated in galvanostatic mode. So the applied current density is set on the current collector surface of the positive electrode and the potential ground boundary is set on the current collector surface of the negative electrode:

$$\int_{\partial\Omega} i_s \cdot \boldsymbol{n} dl = I \int_{\partial\Omega} dl \text{ (positive)} \quad (19)$$
$$\emptyset_{s,ext} = 0 \text{ (negative)} \quad (20)$$

Where I is the average applied current density.

3.3. Numerical Details

The model presented above was solved using the package COMSOL Multi-physics® which is based on the finite-element method. A quadratic basis was used in all of the simulations, together with 1281450 elements. The relative error tolerance is set to 1×10^{-6}. The default set of parameter values is listed in Tables 2–5.

Note that there are not stack shunt current, and the current density entering each cell is equal. In order to match the potential at the beginning of discharge it was necessary to consider the contact resistances between the electrodes and current collectors. A total value of 98 mV was obtained from fitting the experimental to simulation results. The cell stack voltage curve was shifted vertically upwards by this value.

Table 5. Basic operation parameters

Parameter name	Symbols	Value	Unit
Volumetric flow rate	$\vec{v}$	3-7	mm s^{-1}
Electrolyte inlet temperature	T	293.15	K
Electrolyte outlet pressure	P	0	Pa
Applied current density	I	400	A m^{-2}
Cell stack width	W	155	mm
Trapezoidal channel height	h	20	mm
Trapezoidal angle	n	70	°

4. RESULTS AND DISCUSSION

4.1. Validation of the Model

The simulated and experimental values of the cell stack voltage at different soc for applied current density of 10mA/cm^2 is showed in Fig.2. It shows a good agreement for figures between the simulated results and experimental data. The average of relative error is less than 1.15%. The slight error may be caused by the non-consideration of the side-reactions of the electrode and the convective mass transfer in porous electrode.
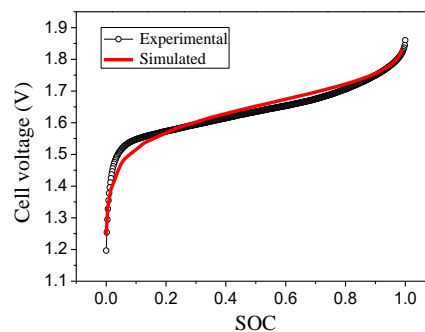
Figure 2. Comparison of experimental and simulation values of cell stack voltage for applied current densities of 10mA/cm^2 at different soc

4.2. Characteristics of Current Density Distribution

The distributions of current density in each cell is similar according to the simulation result. Just as fig.3, the current densities of electrolyte in channel and the negative electrode is evenly distributed, and big change occurs in the positive electrode along x direction. In the porous electrode, the current density of electrolyte increases as the distance from the current collector increases along any horizontal line. The current density of the liquid phase near the current collector is close to 0 mA/cm^2 and is 40 mA/cm^2 near the flow channel. Sun Hong [19] also mentioned a similar rule in the study of vanadium batteries that the distribution of electrolyte current density varies with the position in the porous electrode, and the electrolyte current density is larger near the surface of the proton exchange membrane and is smaller away from the membrane. On the contrary, current density of solid phase decreases as the channel is approached. The data shows that the sum of the current densities of the solid and liquid phases at the same position is equal to 40 mA/cm^2. The study for distributions of the current density along z and y directions is omitted here because of its small change.
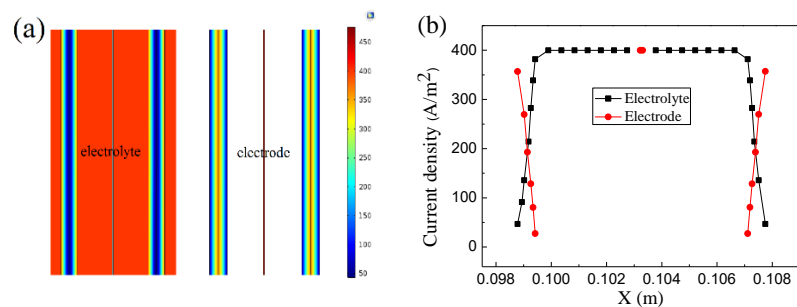
Figure 3. (a) contour plot for distribution of the current density and (b) distribution curves of current density along x direction, for applied current densities of 40mA/cm^2 at 50% soc inside the battery cell 12

4.3. Characteristics of Potential Distribution

The potential distribution in the stack is consistent, i.e. there is little difference of distributions for the electrode potential and the electrolyte potential among the battery cells. The positive potential is 1.64-1.68V, and the negative potential is 0 V, and the electrolyte potential is 1.17-1.23 V. Observing one of the battery cells, the solid phase potential is evenly distributed in the horizontal direction, which can be attributed to the reaction structure and high solid phase conductivity. The liquid-phase potential distribution is macroscopically consistent with Sun [19]. There is a larger potential gradient for electrolyte in the x direction. The electrolyte potential on the negative electrode surface is the highest, 1.2 V, and decreases as the positive electrode is approached. The electrolyte potential on the inner side of the positive electrode is the lowest, 1.17 V. In addition, the gradient of electrolyte potential inside the porous anode is larger.
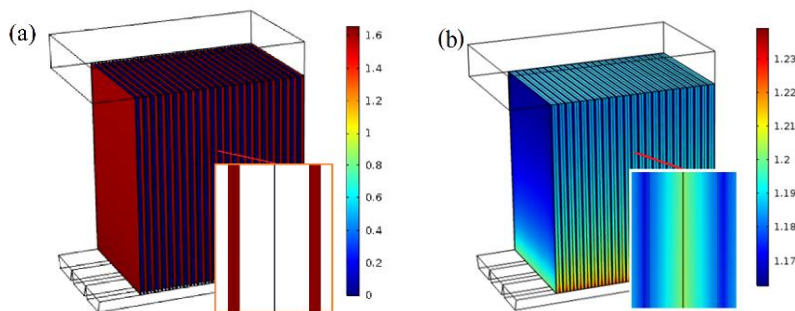
Figure 4. contour plot for distribution of (a)electrolyte potential and (b) electrolyte potential, for applied current densities of 40 mA/cm^2 at 50% soc

The potential of the positive electrode decreases along the z direction which is consistent with the physical phenomenon of the flow cell and is caused by the gradual consumption of reactants in the flow direction. As shown in fig.5(a), from the inlet to the outlet, the positive potential decreases by 27.6-28.7 mV and the negative electrode basically maintains a zero potential. The difference in potentials of the selected battery cells is very small, and the maximum difference is not more than 1.1 mV. In x direction, the battery cell far from the entrance in the stack has a larger solid phase potential and the maximum value of change reached 3.36 mV. This distribution is not affected by the spatial height as showed in fig.5(b) wherein the upper high and lower high are 50 mm from the outlet and inlet of the battery cell, respectively. These are only caused by spatial differences, including uneven distribution of flow rate and concentration in space. Cong [20] considered the stack shunt current for vanadium redox flow battery, and got a similar potential distribution of the electrolyte, but its gradient in space was larger. The distribution of liquid phase potential is similar to that of solid phase potential and is not be discussed here.
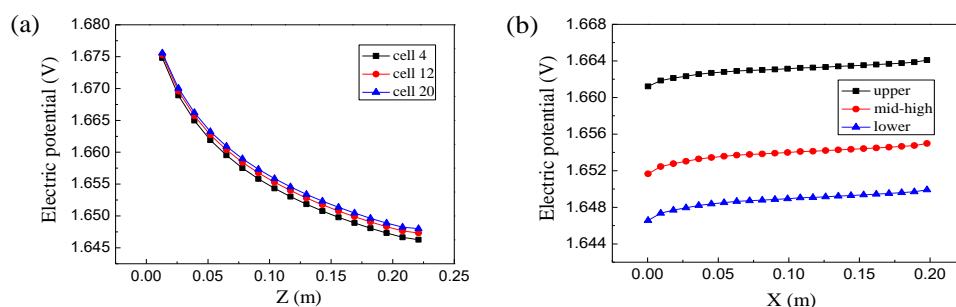
Figure 5. Distributions of (a) electrode potential in the z direction and (b) electrode potential of the cells in x direction of the stack for applied current densities of 40 mA/cm^2 at 50% soc
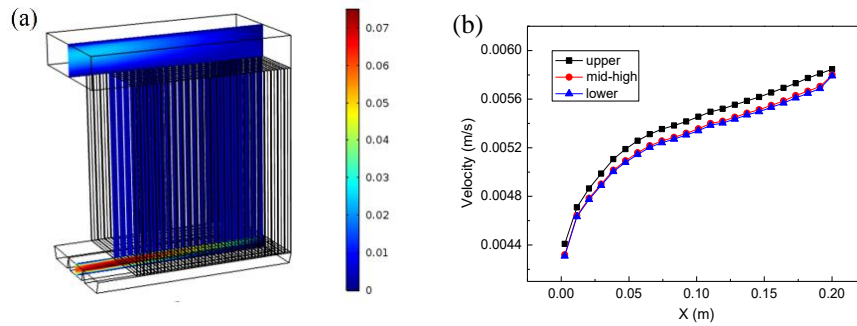
Figure 6. (a) contour plot for distribution of the flow rate and (b) distribution curves of flow rate along x direction of the stack

4.4. Effects of Flow Rate

Figure.6 shows the distribution of flow rate in the stack. The flow in each battery cell is uniform, and is larger at the bottom inlet channel and the top outlet channel. Fig.6(b) shows the flow within each cell of the stack. The greater the distance from the stack entrance, the better the liquidity inside the cell. In comparison, the change in velocity along the flow direction, i.e. z direction, is small and does not need to be considered.

The electrolyte flow rate of zinc–nickel single-flow battery should not to be very high or very low. The suitable flow rate of the electrolyte is between 4.7 L/min and 9.2 L/min [14]. Consequently, on the basis of experimental results, flow rate 0.03 m/s, 0.05 m/s and 0.07 m/s are selected to research. Here, concentration polarization comes up due to the mass transfer limitation, which is created by the reaction concentration gradient between the bulk electrolyte and the electrode surface. It can be described as follow:

$$\beta = \frac{c_i^s}{c_i},$$

where c_i^s is the reactant concentration on electrode surface and c_i is the reactant concentration in the bulk electrolyte.
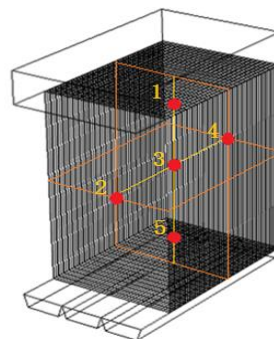
Figure 7. Five positions in the stack
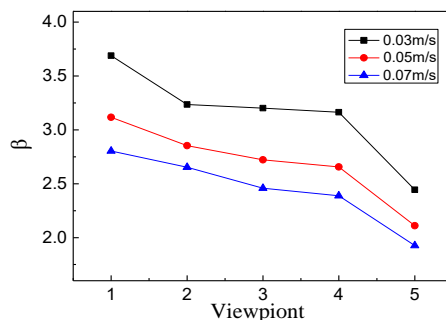
Figure 8. Concentration polarization on the five positions with difference inlet flow rates for applied current densities of 40 mA/cm² at 50% soc

Concentration polarization of zinc ion is the main factor of concentration polarization of zinc-nickel single flow battery. Five positions in the stack were selected, and the concentration polarization was calculated to study the distribution of concentration polarization in the stack. Five positions are selected as shown in fig.7, and the distribution of concentration polarization in the stack is shown in fig.8. The results show that increasing the inlet velocity is beneficial to weaken the polarization degree of ion concentration, especially when the flow velocity is low. The variation of concentration factor at positions 1, 3 and 5 reflects the concentration polarization distribution along the z direction in the stack, and it shows that the ion concentration polarization gradually decreases along the flow direction. At the same flow rate, the difference of β value among positions 1, 3 and 5 is larger, especially when the flow rate is lower than 0.06 m/s, the maximum difference is 1.245. While when the flow rate is higher than 0.06m/s, the difference is smaller, and the value is 0.83-0.935. This shows that the distribution of ion concentration polarization along z direction is more even at higher inlet flow rates. Concentration polarization at positions 2, 3 and 4 reflects the distribution of ions along x direction of the stack. The β value decreases gradually along x direction, that is, the polarization of ion concentration inside the cell far from the entrance of the stack is smaller. At the same flow rate, the difference of β value between positions 2, 3 and 4 is small and decreases with the increase of inlet flow rate, which is opposite to the change of concentration polarization in z direction. In short, increasing the inlet flow rate can effectively reduce the degree of concentration polarization in the stack, and the optimal flow rate should be over 0.06 m/s. Larger flow rate improves the distribution of concentration polarization in z direction, but increases the inconsistency of concentration polarization distribution among cells.

The change on the terminal voltage of the battery cell with the flow rate is shown in fig.9. When the inlet flow rate increases from 0.03 m/s to 0.05 m/s, the voltage increases by 7 mV, and then from 0.05 m/s to 0.07 m/s, the voltage increases by 3 mV. It shows that a higher discharge voltage will be obtained at a large flow rate. And in the study of vanadium batteries [21], it also showed that increasing the flow rate of electrolyte increases the discharge voltage at any given time and prolongs the discharge time. In addition, with the flow rate increasing, the difference in terminal voltage among each cell in the stack increases, and the distribution of terminal voltage tends to be inconsistent, with the maximum difference increasing from 0.55 mV to 3 mV. Therefore, it is necessary to properly control the inlet flow rate of electrolyte and ensure that the inconsistency of the stack voltage distribution is controlled within a reasonable range while pursuing the best electrochemical performance of the stack.
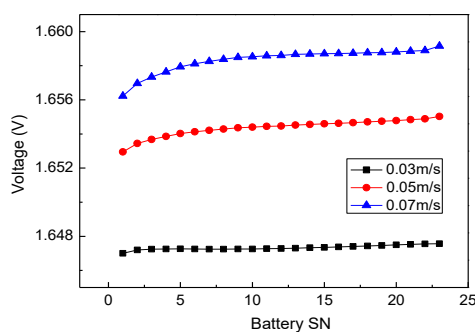
Figure 9. Distribution of the voltage with different inlet flow rates for applied current densities of 40 mA/cm^2 at 50% soc

4.5. Concentration Effects

At any time during the discharge process, the distribution of ions concentration in the stack is similar, as shown in fig.10. The hydroxide ions are generated inside the positive electrode and consumed on the surface of the negative electrode, so from the inside of the positive electrode to the surface of the negative electrode the concentration of hydroxide ions decreases. Zinc ions are generated on the surface of the negative electrode and transferred outward, and the distribution of zinc ions shows a downward trend from the surface of the negative electrode to the inside of the positive electrode. The concentration is evenly distributed in the channel, and the concentration gradient is mainly inside the positive electrode and on the surface of the negative electrode. The hydroxide ion concentration difference between the electrolyte in the anode and the bulk electrolyte is 60-1800 mol/m^3, and the zinc ion concentration difference is negligible The maximum hydroxide ion concentration difference between the negative surface and the bulk electrolyte is 1200 mol/m^3, and the zinc ion concentration difference is 1060 mol/m^3. Fig.10(c) and (d) shows the distribution of ion concentrations on the positive and negative electrode surfaces of different battery cells in the z direction.
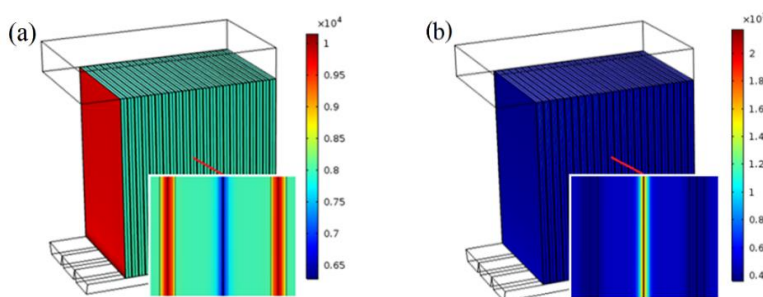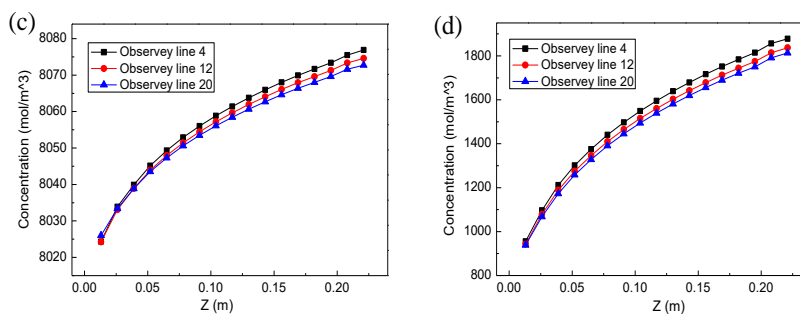
Figure 10. Contour plot for distribution of (a) hydroxide ions and (b) zinc ions, distribution curves of (c) hydroxide ions and (d) zinc ions in different cells along z direction, for applied current densities of 40 mA/cm^2 at 50% soc

The ion concentration increases along the Z direction with the height from the entrance increasing, and the zinc ion concentration increases more greatly. The comparatively larger concentration difference in z direction corresponds to the accumulation of ions along the flow direction. In addition, the concentration distribution of different battery cells is similar, indicating that the concentration distribution of each battery cell in the stack has good consistency. The concentration polarization at different locations in the stack for different inlet concentrations is shown in fig.11. With the inlet concentration of zinc ion increasing, the β decreases obviously and the polarization of ion concentration decreases gradually, and this change is more significant at low inlet concentration. Increasing the inlet concentration of ions also improves the uniformity of concentration polarization distribution in the stack to some extent.
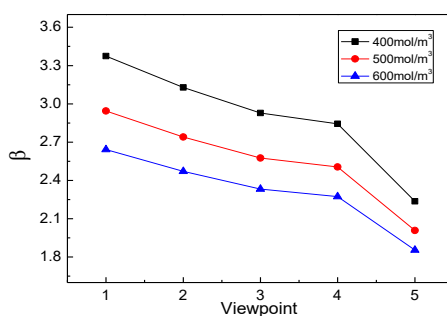
Figure 11. Concentration polarization on the five positions with difference flow rates for applied current densities of 40 mA/cm^2 at 50% soc.

The distribution of cell terminal voltage in the stack for different inlet concentration, as shown in fig.13. The voltage increases with the concentration of inlet ion increasing and this tendency is more pronounced at low inlet concentrations. For every 1000 mol/m^3 increase or decrease in the inlet concentration of hydroxide ion, the average terminal voltage increases or decreases by 3.4-4.6 mV, and for every 100 mol/m^3 increase or decrease in the inlet concentration of zinc ion, the voltage increases or decreases by 2.2-2.5 mV. The comparison shows that the inlet concentration of hydroxide ions has a greater impact on the electrochemical performance of the stack.
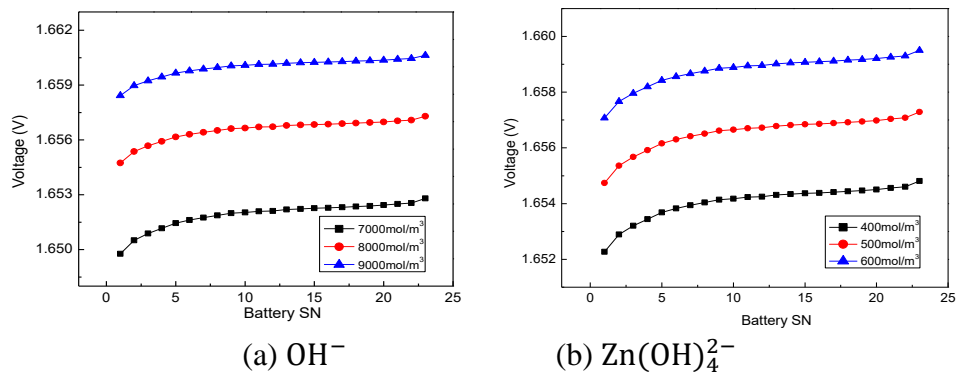
Figure 12. Cell voltage distribution with different ion inlet concentrations for applied current densities of 40 mA/cm^2 at 50% soc.

5. CONCLUSION

A three-dimensional stationary model based on the approaches developed by Xiao [18] has been applied to predict the distributions of current density and potential, and the effects of flow rate and inlet concentration on the performance of the cell stack for zinc-nickel single flow battery. For the distributions of current density and potential, a large gradient exists in each cell along x direction, with the current density gradient mainly in the porous anode and the liquid phase potential gradient mainly in the bulk electrolyte. But for the cell stack, they are uniformly distributed, i.e. there is a good consistency among battery cells. The spatial layout of battery cells has a great influence on the flow rate and concentration, which is reflected in the high inconsistency for the distributions of flow rate and concentration among battery cells. Low flow rate can lead to serious concentration polarization. Increasing the flow rate can significantly improve the concentration polarization and increase the stack voltage, but it will lead to an increase in the inconsistency between the battery cells to some extent. Higher inlet concentration of ions tends to acquire greater cell stack voltage without affecting the inconsistency of the stack, and increasing the concentration of zinc ion can significantly improve the concentration polarization.

The stationary model is simple in programming and can save some solving time without losing much accuracy, especially for large model calculation. The simplified model especially suitable for qualitative analysis. However, stack shunt current and side reactions are not considered, leaving a certain gap between the calculation model and the real one, which needs to be improved in the future work.

References

1. D. Dunyong, Z. Qi, Z. Ping, W. Yuehua, Y. Yusheng, *Chinese Battery Industry*, 16(2011) 56.
2. F. Diaz-Gonzalez, A. Sumper, O. Gomis-Bellmeunt, R. Villafafial-Robles, *Renewable & Sustainable Energy Reviews*, 16(2012) 2154.

3. Vynnycky, M.1michael, *Energy*, 36(2011)2242.
4. Q. Xu, T.S. Zhao, P.K. Leung, *Applied Energy*, 105(2013)47.
5. Y. Cong, G. Yan, G. Shaoyun, T. Hao, *Energy*, 74(2014)886.
6. Z. Qiong, Z. Huamin, X. Feng, M. Xiangkun, L. Xianfeng, N. Guiling, *Applied Energy*, 113(2014)1675.
7. J. Kim, H. Park, Applied Energy, 206(2017)451.
8. Z. Li, C. Jie, Y. Yusheng, W.Yuehua, C. Gaoping, W. Xindong, *Electrochemistry Communications* 9(2007)2639.
9. Z. Li, C. Jie, Y. Yusheng, W.Yuehua, W. Xindong, C. Gaoping, *J. Power Sources*, 179(2008)381.
10. Y. Ito, M. Nyce, R. Plivelich, M. Klein, D. Steingart, S. Banerjee, *J. Power Sources*, 196(2011)2340.
11. C. Yuanhui, Z. Huamin, L. Qinzhi, L. Xianfeng, S. Dingqin, *Electrochim, Acta*, 105(2013)618.
12. C. Yuanhui, L.Qinzhi, L. Xianfeng, X. Xiaoli, Z. Qiong, D. Cong, Z. Huamin, *Electrochim. Acta*, 145(2014)109.
13. C. Yuanhui, X. Xiaoli, L. Dan, L. Xianfeng, L. Qinzhi, Z. Huamin, *RSC Advances*, 5(2015)1772.
14. S. Shiye, P. Junli, W. Yuehua, C. Jie, *Chemical journal of Chinese universities*, 35(2014)134.
15. S. Yindong, W. Yucai, X. Min, Y. Shouguang, C. Jie, H. Ke, Twenty-first national academic conference on engineering thermophysics in colleges and universities (in china), 2015.
16. L. Xuehu, X. Zili, C. Jie, Z. Pengcheng, G. Weidong, World Non-Grid-Connected Wind Power and Energy Conference, (2009)1.
17. Y. Shouguang, L. Peng, X. Min, C. Jie, W. Yucai, *Energies*, 10(2017)1101.
18. X. Min, W. Yucai, Y. Shouguang, S. Yindong, C. Jie, H. Ke, *J. Renewable and Sustainable Energy*, 8(2016):064102.
19. S. Hong, Z. Kaiming, Y. Mingfu, W. Yuhou, J. *Engineering Thermophysics*, 38(2017)568.
20. Y. Cong, G. Shaoyun, F. Honglin, L. Jiayi, L. Yang, T. Hao, *Applied Energy*, 151(2015)237.
21. A.A. Shah, M.J. Watt-Smith, F.C. Walsh, *Electrochim. Acta*, 53(2008)8087.